Interpreting Inverse Correlation Time: from Blood flow to Vascular Network

Qingwei Fang[a], Chakameh Z. Jafari[b], Shaun Engelmann[a], Alankrit Tomar[b], Andrew K. Dunn[a,b,c]

[a]*Department of Biomedical Engineering, The University of Texas at Austin, Austin, 78712, TX, US*
[b]*Department of Electrical and Computer Engineering, The University of Texas at Austin, Austin, 78712, TX, US*
[c]*Correspondence: adunn@utexas.edu*

Abstract

1 The inverse correlation time (ICT) is a key quantity in laser speckle contrast
2 imaging (LSCI) measurements. Traditionally, ICT is regarded as a metric
3 of blood flow, such as speed or perfusion. However, we highlight that ICT
4 not only contains important information about blood flow, but also reflects
5 the underlying structure of the vascular network. In the past, ICT has been
6 found to be correlated with vessel diameter. Here, we further report that ICT
7 exhibits a different sensitivity to blood flow depending on vessel orientation.
8 Specifically, ICT is more sensitive to blood flow speed changes in vessels de-
9 scending from or arising to the tissue surface, compared with those laying
10 parallel to the surface. Those findings shift our understanding of ICT from
11 purely blood flow to a combination of blood flow and vascular network struc-
12 ture. We also develop theories to facilitate the study of vascular network's
13 impact on ICT.

Keywords: dynamic light scattering, laser speckle contrast imaging, inverse
correlation time, blood flow, vascular network
PACS: 0000, 1111
2000 MSC: 0000, 1111

1. Introduction

15 Laser speckle contrast imaging (LSCI) has gained attention in recent years
16 for the quantification of blood flow in biomedical imaging applications[1-3]. It

17 is non-invasive, non-ionizing and label free. In general, the higher the blood
18 flow speed, the more rapidly the speckle patterns will vary in time, leading to
19 a lower speckle contrast when integrated over the camera exposure time[4,5].
20 Valuable information about blood flow perfusion in regions of interest can be
21 extracted in real time from the continuous and wide-field 2-dimensional (2D)
22 monitoring of speckle contrast[6,7]. Nevertheless, the speckle contrast only
23 provides qualitative measurements of the underlying blood flow[8]. Numerous
24 efforts have been put into advancing LSCI from qualitative to a quantitative
25 imaging modality[9–15].

26 One promising path is to relate speckle contrast to the autocorrelation
27 function of detected electric field, $g_1(\tau)$ and extract the inverse correlation
28 time (ICT) as the index of blood flow. Within a limited set of conditions, ICT
29 is proportional to the typical speed of blood flow within a certain range[16,17],
30 and it has demonstrated great potential in quantifying cerebral blood flow
31 and facilitating intraoperative flow monitoring[18–21].

32 In view of the promise of ICT in transforming LSCI to a quantitative
33 imaging modality, the strategy to extract ICT from measured speckle dy-
34 namics is gaining the significant attention. Initially this was done with
35 single-exposure LSCI[16,17], and more recently, multi-exposure speckle imaging
36 (MESI) was developed to extract ICT more accurately from the confounding
37 effects of static scattering, instrumentation noise and loss of correlation due
38 to speckle averaging[22–24]. Recently, dynamic light scattering imaging (DLSI)
39 was proposed to reduce the ICT estimating error owing to an inaccurate
40 model of electric field autocorrelation function[25].

41 Though ICT has been mainly interpreted as a metric of blood flow, such
42 as speed, or perfusion, there is increasing evidence that ICT is subject to the
43 structure of the vascular network. Kazmi et al.'s experimental results showed
44 that ICT might be quantifying neither volumetric flux nor flow speed but the
45 product of the flow speed and vessel diameter[26]. Fredriksson et al. reported
46 the vessel packaging effect in which the confinement of blood to vessels with
47 an average diameter of $40\,\mu$m could lead to a 50% reduction in perfusion
48 estimation by LSCI compared with homogeneous blood distribution inside
49 the tissue[27]. Jafari et al. found that ICT could be shifted over 10 times
50 under the homogeneous assumption compared with using the actual vascular
51 geometry, highlighting the significant impact of vascular geometry on ICT[28].

52 The impact of vessel orientation on ICT has not been fully investigated
53 yet. In this work, we conducted Monte Carlo simulations and found that ICT
54 of vessels perpendicular to the tissue surface, i.e. descending from/arising to

2

the surface, exhibits a higher sensitivity to blood flow changes than that of vessels laying on the surface. Such finding is confirmed by experimental validation *in vivo* combining MESI and 2-Photon (2P) imaging. Those results suggest that the structure of the underlying vascular network deserves more attention than it currently receives in the interpretation of ICT. We also develop a generalized theory to facilitate the study on the impact of vascular network structure. It is compatible with all extant $g_1(\tau)$ models and free of assumptions about groundtruth blood flow speeds.

2. Theory and Methods

2.1. A unified theoretical framework for ICT interpretation

According to the traditional dynamic light scatteirng (DLS) and diffusing wave spectroscopy (DWS) theories, in different scattering regimes (single vs. multiple) and flow conditions (ordered vs. unordered), different assumptions should be made about the form of the electric field autocorrelation function $g_1(\tau)$ [29–33], as shown in **Fig. 1A** [25]. τ_c is the correlation time and ICT is defined as $1/\tau_c$. The modulation number n is the main differentiating factor among those models.

In this paper, we first introduce a unified theoretical framework that is compatible with all extant $g_1(\tau)$ models. After Monte Carlo simulation of photon migration inside the tissue, the electric field auto-correlation function $g_1(\tau)$ can be calculated according to Eq. 1 (ref. [34])

$$|g_1(\tau)| = \left| \int_{-\infty}^{\infty} \mathrm{P}(Y) e^{jY\tau} dY \right| \tag{1}$$

where $Y = \sum_{i=1}^{N} \vec{q_i} \cdot \vec{v_i}$ and $\vec{q} = \vec{k_o} - \vec{k_i}$. N is the number of dynamic scattering events experienced by a single photon. N can be larger than 1 hence Eq. 1 accommodates both single and multiple scatter regimes. $\vec{q}$ is the momentum transfer vector defined as the difference between the scattering wave vector $\vec{k_o}$ and the incident wave vector $\vec{k_i}$ [35]. The direction of $\vec{k_o}$ and $\vec{k_i}$ is the propagating direction of the scattered light and incident light, respectively. The amplitudes are both equal to k_0, the wavenumber. Finally, $\vec{v_i}$ is velocity of the scattering particle in the i-th dynamic scattering event experienced by the photon. For clarity sake, speed refers to scalars while velocity corresponds to vectors in this paper. Note that since the instantaneous velocity of Brownian particles is physically measurable[36], we expand the definition of

3

$\vec{v}_i$ from the velocity of ordered motion as defined in ref. [34] to include both ordered and diffusive motions. $P(Y)$ is the probability density function of Y. When some photons generate the same Y value, their weights will be added together to give rise to $P(Y)$. Y can be interpreted as the accumulation of frequency shifts induced by dynamic scattering (see Supplemental Material section 1 for a more concise proof than ref. [37]).

$$g_1(\tau) = \int_{-\infty}^{\infty} \Omega(\omega) e^{j\omega\tau} d\omega \tag{2}$$

With $g_1(\tau)$ rewritten in terms of Y, we notice that $g_1(\tau)$ is the Fourier transform of $P(Y)$. Considering the Wiener-Khintchine theorem, if $\Omega(\omega)$ is the normalized power spectral density of the detected electric field, then $g_1(\tau)$ would be the Fourier transform of $\Omega(\omega)$ (Eq. 2) (ref. [38]). Therefore, we arrive at Eq. 3 that $P(Y)$ is a shifted version of $\Omega(\omega)$

$$\Omega(\bar{\omega}) = P(Y) \tag{3}$$

where $\bar{\omega} = Y + \omega_0$ and ω_0 is the center frequency of the electric field.

Substituting $P(Y)$ for $\Omega(\omega)$ is advantageous in that $P(Y)$ reveals the mechanism of spectrum broadening in LSCI since Y is the accumulation of frequency shifts induced by dynamic scattering. $P(Y)$ and specific forms of $g_1(\tau)$ can be bridged by Eq. 4 and 5. For $g_1(\tau) = e^{-|\tau|/\tau_c}$,

$$\frac{1}{\tau_c} = \Gamma \tag{4}$$

where Γ is the half width at half maximum of the Lorentzian $P(Y) = \frac{1}{\pi\Gamma}\left(\frac{1}{1+\frac{Y^2}{\Gamma^2}}\right)$. For $g_1(\tau) = e^{-(\tau/\tau_c)^2}$,

$$\frac{1}{\tau_c} = \frac{1}{\sqrt{2}}\sigma \tag{5}$$

where σ is the standard deviation of the Gaussian $P(Y) = \frac{1}{\sqrt{2\pi}\sigma}e^{-\frac{Y^2}{2\sigma^2}}$. See proof in Supplemental Material section 2.

These two equations (Eq. 4 and 5) provide new interpretations of ICT (i.e., $\frac{1}{\tau_c}$) from the point of view of $P(Y)$. For Lorentzian $P(Y)$, ICT determines the half width at half maximum while in Gaussian $P(Y)$, ICT is a scaled version of the standard deviation. Note that in both cases, ICT serves as a kind of measure of the broadening of the spectrum of Y. In fact, as long

4

112 as the spectrum of detected light is both bandwidth- and amplitude-limited,
113 a more general linear relationship

$$114 \qquad (\tfrac{1}{\tau_c})^2 \propto \mathrm{Var}\,(Y)$$

115 can be shown to hold for any electric field auto-correlation functions taking
116 the form of $g_1(\tau) = e^{-(|\tau|/\tau_c)^n}$ (see Supplemental Material section 3 for proof).
117 This suggests that ICT in the various $g_1(\tau)$ models shown in Fig. 1a can be
118 unified as the reduced case of the standard deviation of Y. Since $\mathrm{P}\,(Y)$
119 is essentially the same as the power spectral density of the electric field of
120 detected light (Eq. 3), ICT can be interpreted as the scaling factor of the
121 variance of the detected optical spectrum as well. Since $\mathrm{Var}\,(Y)$ measures
122 the variance of frequency shifts in the dynamics scattering process, we call it
123 the variance of dynamic scattering.

124 *2.2. Characterizing the inherent properties of vascular network to produce*
125 *ICT*

126 In this section, we aim to decouple the effects of blood flow speeds and
127 vascular structure on ICT and develop tools to study the vascular network
128 individually. Further analyzing the structure of Y and separate the contri-
129 butions to Y by the blood flow and others, we arrive at Eq. 6

$$Y = Y_s + Y_f = Y_s + k\widetilde{v} \qquad (6)$$

130 where Y_f represents the contributions to Y by motions induced by blood flow
131 while Y_s denotes the component in Y that is independent of the blood flow.
132 Y_f can be expressed as the product of k and $\widetilde{v}$ where $k = \sum_{i=1}^{N} |\vec{q_i}| \cos \alpha_i$,
133 $\widetilde{v} = \frac{\sum_{i=1}^{N} |\vec{q_i}| \cos \alpha_i \cdot |\vec{v_i}|}{\sum_{i=1}^{N} |\vec{q_i}| \cos \alpha_i}$ and α_i is the angle between $\vec{q_i}$ and $\vec{v_i}$. The $\vec{q_i}$, $\vec{v_i}$ and N
134 follow same definition as in Eq. 1.

135 Note that $\widetilde{v}$ represents the weighted average of absolute blood flow speeds
136 and the weighting is determined by the photon's scattering geometry, i.e., the
137 scattering angle and the angle between the momentum transfer vector $\vec{q_i}$ and
138 velocity vector $\vec{v_i}$. k is the sum of weights and equal to Y_f when blood flow
139 speeds are all unit speeds.

140 Also notice that k and $\widetilde{v}$ are well de-correlated from each other. To under-
141 stand this, it is helpful to view k as the sum of weights and $\widetilde{v}$ as the weighted
142 average of blood flow speeds. When the sum of weights changes, we would
143 not be able to predict how the weighted average will change if little is known
144 about how the individual weight changes. The weighted average can increase

5

or decrease. It can also remain invariant if the weights increase/decrease by the same ratio.

Furthermore, if we assume that blood flow speeds are uncorrelated with the photon's scattering geometry (i.e., the scattering angle and the angle between $\vec{q_i}$ and $\vec{v_i}$ are uncorrelated with the magnitude of the flow vector), $\widetilde{v}$ and k would be uncorrelated (see proof in Supplemental Material section 4). With this uncorrelated relationship, we arrive at Eq. 7 and 8

$$\mathrm{E}\left(Y\right) = \mathrm{E}\left(Y_s\right) + \mathrm{E}\left(k\right)\mathrm{E}\left(\widetilde{v}\right) \tag{7}$$

$$\mathrm{Var}\left(Y\right) = \mathrm{Var}\left(Y_s\right) + \mathrm{Var}\left(k\right)\mathrm{E}\left(\widetilde{v}^2\right) + \mathrm{E}^2(k)\mathrm{Var}\left(\widetilde{v}\right) \tag{8}$$

where $\mathrm{E}\left(X\right)$ and $\mathrm{Var}\left(X\right)$ give the expectation and variance of the random variable X, respectively.

Eq. 7 and 8 points out the relationship between statistical properties of Y and those of k and $\widetilde{v}$. Further approximations to Eq. 8 can be made to accommodate blood flow quantification. Either of the following two conditions is sufficient for Eq. 9 to be applied with good accuracy. First, the vascular structure sampled by detected photons is dominated by a single vessel, i.e., $\mathrm{Var}\left(\widetilde{v}\right)$ is approximately 0. This is true for major surface vessels where dynamic scattering events of detected photons are strongly localized within that vessel[8,21,33]. Second, the scattering of collected photons is fully randomized, i.e., $\mathrm{E}\left(k\right)$ is 0. This is true for parenchyma regions where dynamic scattering is dominated by micro-vessels whose orientation is randomized. Our simulation results of $\mathrm{E}\left(k\right)$ on parenchyma regions also support that as section 3.1 will show.

$$\mathrm{Var}\left(Y\right) = \mathrm{Var}\left(Y_s\right) + \mathrm{Var}\left(k\right)\mathrm{E}\left(\widetilde{v}^2\right) \tag{9}$$

With Eq. 9, we define the characteristic variance of dynamic scattering as $\mathrm{Var}\left(k\right)$. If we plot Eq. 9 (Fig. 2), the physical implications of $\mathrm{Var}\left(k\right)$ are evident as the slope. $\mathrm{Var}\left(k\right)$ can be defined for each detection point (i.e., a pixel on the camera) in LSCI and it characterizes the ability of the sampled vascular network to decrease speckle contrast or increase ICT under the specified illumination/detection setup at the detection point. The larger the $\mathrm{Var}\left(k\right)$, the stronger the ability of the vascular network to decrease speckle contrast or increase ICT under the same blood flow speed, at the detection point. In addition, $\mathrm{Var}\left(k\right)$ is independent of the blood flow speed since it

176 is defined with unit speeds. Hence, it reveals the inherent properties of the
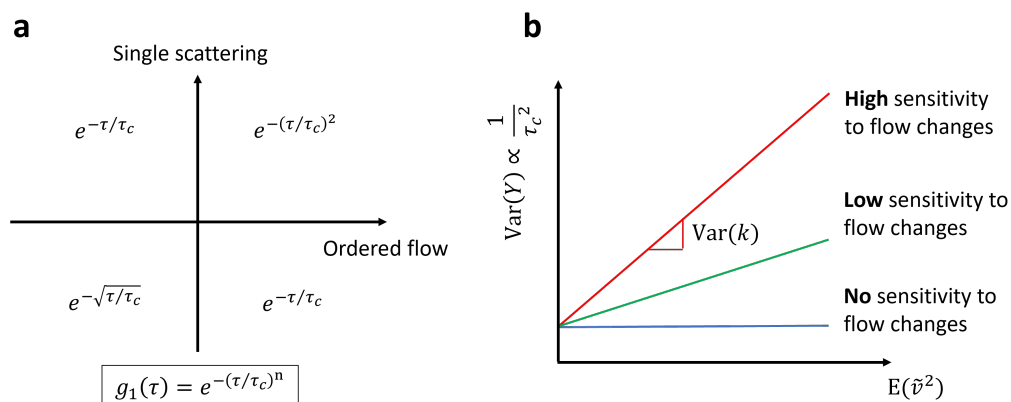177 vascular network under the specified illumination/detection setup.

Figure 1: **A unified theoretical framework for ICT interpretation. a** The various $g_1(\tau)$ models proposed in treatment of the complex vascular network in LSCI. Extant models of the electric field auto-correlation function in various cases of scattering regimes and flow conditions. τ_c is the correlation time and ICT is defined as $1/\tau_c$. On the quadrant plot, the opposite of the order motion is unordered motion (also known as diffusive motion) and that of single scattering is multiple scattering. **b** Physical meaning of the characteristic variance of dynamic scattering. The vertical axis depicts the variance of dynamic scattering $\mathrm{Var}\,(Y)$ which is proportional to the square of ICT. The horizontal axis is the weighted average of blood flow speeds sampled by the photon scattering process. The slope of the plot is $\mathrm{Var}\,(k)$. A steeper slope indicates a vascular network of higher sensitivity to flow changes.

2.3. Monte Carlo simulation

179   The simulation algorithm is based on ref. [28]. The uniform flat beam
180 profile is used for simulation. The effects of ordered motion of the RBCs
181 along the direction of vessels are investigated in this study. Though the
182 diffusive motion of RBCs has been recently suggested as dominating the
183 correlation decay in diffuse correlation spectroscopy (DCS) measurements[39],
184 it is unclear whether the effects are due to the radially diffusive motion of
185 RBCs within vessels or axially ordered motion of RBCs along the vessel but
186 within a diffusive vascular network where vessels are curved and direction-
187 randomized. Nor it is clear whether the observation holds in LSCI. Jafari et
188 al. found that the axially ordered motion of RBCs along the vessel adequately
189 describes the particle dynamics in LSCI given the strong agreement between

7

experimental and simulated speckle contrast values[28].Hence, the effects of radially diffusive motion of RBCs within vessels might be negligible in LSCI. The potential impact of radially diffusive motion of RBCs within vessels to findings of this study is also discussed in section 4.1.

The simple vascular geometry for simulation is made of parallel and equally spaced vessels (similar to ref. [39]). Vessels in the first geometry are parallel to y axis, and parallel to z-axis in the second geometry (Fig. 2a). Some of the major settings are as follows: geometry size: $1 \times 1 \times 1 \, \text{mm}^3$, the radius of vessels: 0.01 mm, space between vessels: 0.1 mm, radius of the incident beam: 0.25 mm, radius of the detector: 0.01 mm, NA of the detector: 0.2. The detector is placed in the center of the field of view and right above the vessels. The optical properties of vessels and tissue are the same as in ref. [39].

For the realistic vascular geometry (shown in Fig. 2b), the simulation flow for generating the photon trajectories through the 3D geometry is detailed by Jafari et al.[28]. Briefly, parallelized Dynamic Light Scattering Monte Carlo (DLS-MC) simulations were launched on the Stampede2 Skylake compute nodes on Texas Advanced Computing Center (TACC) using the Message Passing Interface (MPI) protocol to simulate 80×10^9 photon trajectories through the geometry.

The realistic vascular geometry was obtained through 2P imaging, followed by vectorization of the vascular structure[40]. The vectorized geometry was voxelized into a three-dimensional matrix of the size $277 \times 277 \times 303$ voxels in the X, Y, and Z directions, respectively. The voxel size was a cubic $2 \times 2 \times 2 \, \mu\text{m}^3$, yielding a total geometry size of $554 \times 554 \times 606 \, \mu\text{m}^3$. A circular collimated wide-field beam with a flat profile was set to illuminate 95% of the top surface of the geometry. A NA of 0.25 and detector size of $9.8 \times 9.8 \, \mu\text{m}^2$ were used in the simulation settings to reflect the typical configuration of LSCI experimental setup. For detected photons, both entry and exit locations as well as the photon trajectories through the volume and photon weights were recorded. The optical properties of capillaries, non-capillary vessels and extra-vascular tissue as used in ref. [28] are adopted.

2.4. In vivo experimental validation

The MESI imaging system detailed in ref. [21, 22] is used for microfluidics and *in vivo* speckle imaging experiments. The laser wavelength is 785 nm and the magnification of the system is 2x. 56 MESI sequences with each sequence containing 15 speckle contrast images corresponding to 15 exposure times are
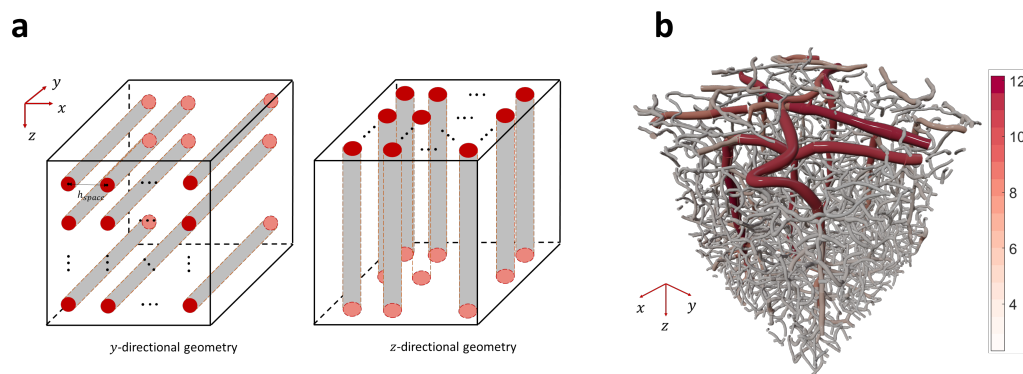
Figure 2: **Vascular geometry in Monte Carlo simulation.** **a** The diagram of simple y- and z-directional vascular geometry. **b** The realistic vascular geometry scanned from a mouse's cerebral cortex. The geometry size is $554 \times 554 \times 606 \, \mu m^3$. 3D rendering by Blender 2.81 (ref. [41]). Color coded by vessel radius (unit: μm).

acquired. The K^2 curves are calculated by averaging speckle contrast values over multiple MESI sequences and then squaring it. ICT values are then extracted by fitting the K^2 curves based on the MESI model[22].

The mouse cranial window preparation procedures were detailed by Kazmi et al.[26]. During imaging sessions, the mouse (C57BL/6, Charles River Laboratories Inc.) was anesthetized with medical grade O_2 vaporized isoflurane (3% induction, 1.5% maintenance).

For 2P imaging, images were acquired with a custom microscope and laser system[42,43]. The same anesthesia procedure as above-mentioned was used. In addition, 100 μL of 70 kDa dextran-conjugated Texas Red diluted in saline at a 5% w/v ratio was added to the blood plasma through retro-orbital injection prior to imaging. The dye was then excited by an Yb fiber amplifier ($\lambda = 1060 \, nm$). 30 frames acquired with a resonant scanner were averaged at each depth to produce images.

All animal procedures in this study were approved by The University of Texas at Austin Institutional Animal Care and Use Committee (IACUC).

3. Results

3.1. Monte Carlo Simulation

The simulation results on the realistic vascular network under normal illumination are shown in Fig. 3. Figure 3a-e shows the map of the number of

9

247 detected dynamic photons (i.e., photons experiencing dynamic scattering at
248 least once), $\mathrm{Var}(k)$, $\mathrm{E}(k)$, and $\mathrm{Var}(Y)$, respectively. To counter the effects of
249 wavelength, the $\mathrm{Var}(Y)$, $\mathrm{Var}(k)$ and $\mathrm{E}(k)$ are normalized by the wavenum-
250 ber, i.e. $\mathrm{Var}(Y/k_0)$, $\mathrm{Var}(k/k_0)$ and $\mathrm{E}(k/k_0)$, unless specified otherwise.
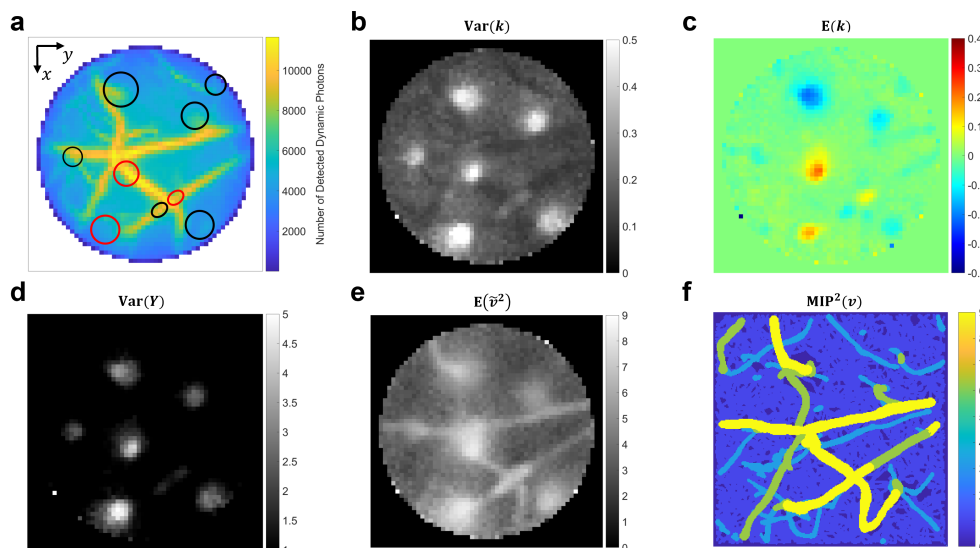

Figure 3: **Simulation results on the realistic vascular network under normal illumination. a** The map of the number of detected dynamic photons at each camera pixel. The dynamic photons refer to photons which experience at least one dynamic scattering event before exiting and being detected. **b-f** The map of $\mathrm{Var}(k)$, $\mathrm{Mean}(k)$, $\mathrm{Var}(Y)$, $\mathrm{E}(\tilde{v}^2)$, and $\mathrm{MIP}^2(v)$, respectively. $\mathrm{MIP}^2(v)$ represents the square of maximum intensity projection of flow speeds assigned in simulation. The position of bright spots in (**b**), (**c**) and (**d**) is circled out correspondingly in (**a**).

251 There are several interesting observations. First, note the bright blobs in
252 Fig. 3b, d and blue/orange blobs in Fig. 3c whose positions are circled in Fig.
253 3a. The reason that those blobs appear in those places instead of elsewhere
254 is suspected to be correlated with the underlying vascular structure and we
255 find that there is always a major descending/ascending vessel in those spots
256 (Fig. 2b and Supplemental Material section 5).

257 Second, the major surface vessels extending in the x-y plane shown in Fig.
258 3a appear even darker than surrounding parenchyma regions in the $\mathrm{Var}(k)$
259 map (Fig. 3b). This suggests that $\mathrm{Var}(k)$ might be sensitive to the orien-
260 tation of vessels, namely, small for x-y plane surface vessels while large for

10

z-directional descending vessels under normal illumination. This hypothesis is verified by simulation results on the simple vascular geometries consisting of parallel and equally-spaced vessels. $\mathrm{Var}\,(k)$ of z-directional vessels is observed to increase by 7 times compared with that of y-directional vessels under normal illumination (Supplemental Material section 6).

Third, among those blobs, some are blue while others appear orange in Fig. 3c. Further analysis on the flow vector assignment in simulation reveals that this is dependent on whether the flow vector is z-positive or z-negative (Supplemental Material section 7).

Finally, $\mathrm{E}\,(k)$ of parenchyma regions is 0 (Fig. 3c). Hence, Eq. 9 can be applied with good accuracy. With $\mathrm{Var}\,(Y_s)$ being 0 in simulation, we could calculate $\mathrm{E}\,(\widetilde{v}^2)$ by dividing $\mathrm{Var}\,(Y)$ with $\mathrm{Var}\,(k)$. As Fig. 3e shows, the $\mathrm{E}(\widetilde{v}^2)$ map reveals a clearer structure of surface vessels than $\mathrm{Var}\,(Y)$ (Fig. 3d). To evaluate accuracy of the absolute blood flow speed estimation given in Fig. 3e, the square of the maximum intensity projection (MIP) of blood flow speeds assigned in simulation is mapped in Fig. 3f. In terms of the resolved vessels, the shape of x-y plane surface vessels is well preserved in Fig. 3e and the intensity value also shows a good match with that in Fig. 3f. However, for z-directional descending vessels, the vessel boundary is expanded and there is no clear border, which highlights their distinct properties in LSCI from x-y plane surface vessels.

3.2. Experimental validation

The enhanced sensitivity of speckle contrast to blood flow speed in z-directional vessels compared with x-y plane vessels is also observed *in vivo*. As highlighted by white arrows in Fig. 4a and b, the orthogonal X-Y and X-Z cross-sections of 2P imaging data clearly reveal an inverted "L" shaped vessel. At the end of its surface strand, it develops into a descending strand into the tissue. ROI of the two strands is shown by the white boxes in Fig. 4d. Notice that there is no other major vessel branch on this "L" shape and vessel diameters of the two strands are approximately the same. Thus, based on blood flow conservation[26], the flow speed should be approximately the same in these two strands. Nevertheless, we see a lower speckle contrast in areas corresponding to the descending strand as pointed out by the white arrow in Fig. 4c. It indicates an enhancement of the sensitivity of speckle contrast to blood flow speed in the descending strand compared with surface strand. More specifically, the average ICT squared of the descending strand is ∼78% larger than that of its surface counterpart, as highlighted by white
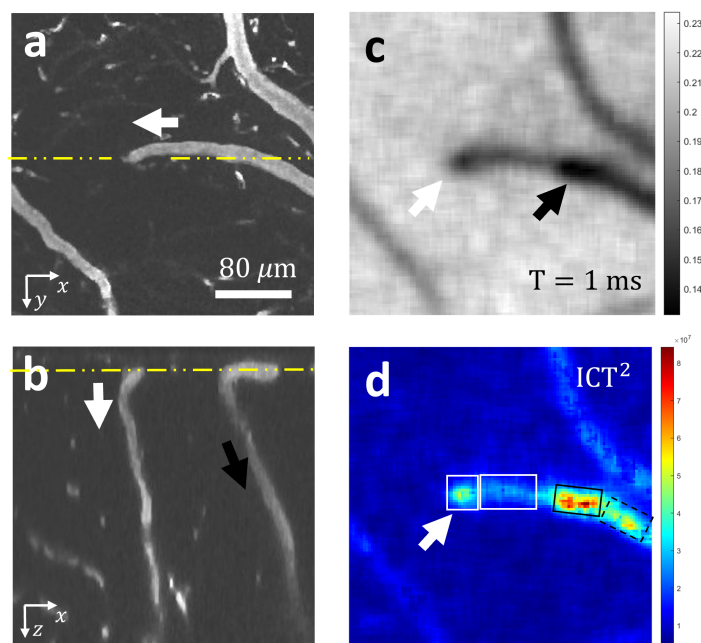
11

Figure 4: **One example of the z-directional descending vessel inducing a more significant decrease of speckle contrast and increase of ICT than its upstream x-y plane surface strand *in vivo*. a**, **b** Orthogonal cross-sections of the vascular structure acquired from 2P imaging. (**a**) X-Y cross-section (depth: $27\,\mu$m); (**b**) X-Z cross-section along the yellow dashed line in (**a**). The yellow line in (**b**) indicates the z position of (**a**). White arrows in (**a**) and (**b**) indicate the direction of an upside-down "L" shaped vessel which has a surface strand extending horizontally on the surface followed by a descending strand deep into the tissue. scale bar: $80\,\mu$m. The spatial scale along the x- and z-axis is the same in (**b**). **c** Single-exposure speckle contrast image of the vascular network. Camera exposure time T=1 ms. The white arrow indicates position of the descending vessel strand which shows a stronger decrease of speckle contrast than its connected x-y plane surface strand. **d** The map of ICT square. The two white boxes highlight the descending strand and surface strand, respectively. The white arrow indicates the position of the descending strand exhibiting a larger ICT value than its connected x-y plane counterpart. The black arrow in **b** highlights another descending vessel branch from the main vessel. The black arrow in **c** and black boxes in **d** indicate the compound effects of vascular structure and blood flow in modulating speckle contrast and ICT values.
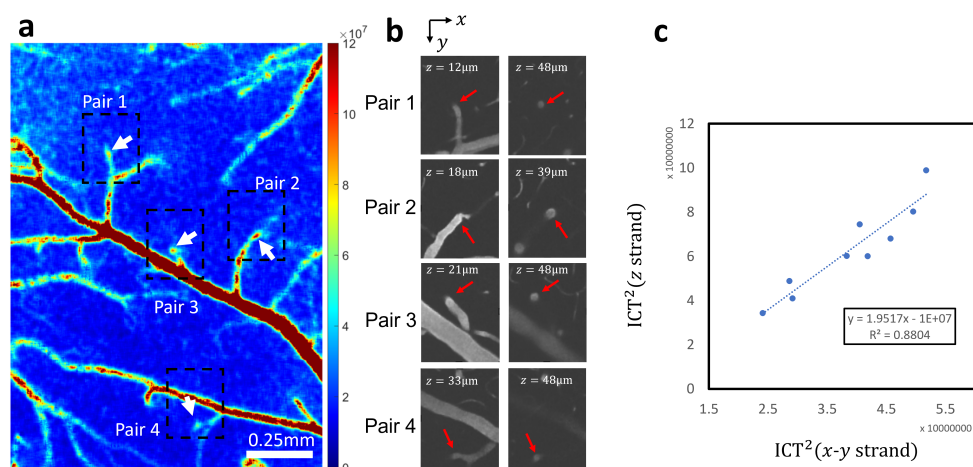
12

Figure 5: **Statistical comparison of ICTs between the z-directional descending vessel strand and its upstream x-y plane surface strand *in vivo*. a** Pairs of z strand and x-y strand in a typical mouse cerebral window whose position is highlighted by the dashed rectangle on the ICT squared image. The arrows point to the descending vessel in each pair. Scale bar: 0.25mm. **b** The corresponding 2P images showing the vascular structure of the four pairs of z strands and x-y strands. The first column shows the X-Y cross-section of the vascular structure near the surface while the second column shows the cross-section at the same location but in a deeper tissue. The red arrows point to the z strands in the pair. **c** The juxtaposing of ICT squared of the z strand and that of the contiguous x-y strand. The scatter plot shows the data of nine z and x-y strand pairs from three mice. The linear fitting is performed and the slope is around 2, larger than 1, which indicates that the ICT of z-directional vessels could be larger than that of x-y plane vessels even though they assume the same blood flow speed. The difference between ICT squared of the z strand and that of the paired x-y strand is statistically significant (paired t-test, n=9, $p < 0.001$).

13

boxes in Fig. 4d). If the impact of $\mathrm{Var}(Y_s)$ is negligible, it implies that $\mathrm{Var}(k)$ of the descending strand would be more than 75% larger than that of surface strand. Notably, similar border expansion is also observed here in the position of the descending strand as in simulation (Fig. 3e).

To further evaluate the statistical significance of the enhanced sensitivity, 9 pairs of z-directional vessels and x-y plane vessels from 3 mice are analyzed. Those vessel pairs are selected for analysis because their vascular structure has the same properties as in the example mentioned above, i.e., the upside-down L vessel shape and the approximately same diameter of the two strands. The location of four z and x-y strand pairs in a typical mouse cerebral window is shown in Fig. 5a and their vascular structure is acquired by 2P imaging (Fig. 5b). ROI of the z and x-y strands in each pair is selected in the similar way as shown by white boxes in Fig. 4d. The ICT squared of the z strand in each pair is plotted against that of the x-y strand (Fig. 5c). The linear fitting results in a slope of approximately 2. In addition, the difference between ICT squared of z strand and that of its contiguous x-y strand is statistically significant (paired t-test, n=9, $p < 0.001$). Those results provide direct experimental evidence for the enhanced sensitivity of ICT to blood flow changes in z-directional vessels compared with vessels extending in the x-y plane.

Finally, the compound effects of vascular structure and blood flow should be noticed. As highlighted by the black arrow in Fig. 4b, there is another descending vessel branch from the main vessel. The blood flow in the main vessel splits into two portions: one goes into the above-mentioned inverted "L" shaped vessel and the other goes into this second descending vessel. Therefore, the speckle contrast and ICT in the solid black rectangle in Fig. 4d result from not only an underlying descending vessel but also the larger blood flow in the main vessel. That is why they are not directly comparable with those of the descending strand in the white square in Fig. 4d. Interestingly, the enhanced sensitivity can be roughly examined if we compare the ICT squared in the solid-line black rectangle with that in the dashed black rectangle in Fig. 4d. Both areas cover the main vessel of the largest blood flow but the solid rectangle assumes larger ICT squared, which indicates the additional impact of the descending vessel in the solid square. Similarly, the joint effects of vascular structure and blood flow are observed in the region of vessel pair 2 in Fig. 5a where a second descending vessel is also present (Fig. 5b).

14

4. Discussion

4.1. Bridging ICT to physiologically meaningful blood flow variables

Given the volume integrated nature of LSCI and the complexity of the vascular network, it has been long hypothesized that if LSCI is measuring some physiologically meaningful blood flow variable, it measures the weighted average of that variable within the probed volume [22, 39]. However, it is unclear how the weighting is determined. Our derivation in section 3.1 and 3.2 reveals that the weighting is determined by photons' dynamic scattering process, according to the definition of $\widetilde{v}$ (Eq. 6). Note that $\widetilde{v}$ is physiologically meaningful and represents the weighted average of blood flow speeds probed by detected photons. In the case that all dynamic scattering events sample the same blood flow speed v, $\widetilde{v}$ would be equal to v regardless the weighting.

Combining the results in section 2.1 and 2.2, a general relationship between ICT and physiologically meaningful blood flow variables, i.e. $\widetilde{v}$, can be established. In section 2.1, it has been shown that ICT squared is proportional to the variance of Y, which accommodates all current $g_1(\tau)$ models in LSCI. In section 2.2, Eq. 9 further points out that the variance of Y assumes a linear relationship with the expectation of $\widetilde{v}$ squared. Hence, the linear relationship between ICT squared and the expectation of $\widetilde{v}$ squared is reached by our theoretical derivation.

Contrary to the frequently adopted notion that ICT is proportional to blood flow speed, our theory concludes that the squares of the two that are linear to each other. The difference between the two notions is centered on whether $\mathrm{Var}\,(Y_s)$ is zero or not. Pragmatically, the existence of $\mathrm{Var}\,(Y_s)$ is indispensable to tackling the "biological zero" problem which refers to the non-zero residual signal even when no blood flow is present[37,44]. A non-zero $\mathrm{Var}\,(Y_s)$ might reduce the difference of ICT values between descending/ascending vessels and surface vessels. As observed in simulation, the $\mathrm{Var}\,(k)$ of z-directional vessels is 7 times larger than that of y-directional vessels in the simple vascular geometry, which is expected to generate a ICT squared difference of 7 times according to Eq. 9 if $\mathrm{Var}\,(Y_s)$ is zero. However, ICT squared *in vivo* is only 60% larger on average in descending/ascending vessels than vessels laying on the surface. A non-zero $\mathrm{Var}\,(Y_s)$ *in vivo* could play a significant role in accounting for such discrepancy. In addition, the scatters' movement could be more diverse *in vivo* compared with our settings in simulation. For example, the radially diffusive motion of RBCs in vessels is not present in our simulation.

$\text{Var}(k)$ plays a major role in bridging ICT and the physiologically meaningful blood flow variable, $\widetilde{v}$, as Eq. 9 points out. It provides a theoretical basis for extracting the physiologically meaningful blood flow variable $\widetilde{v}$ from ICT. Given the $\text{Var}(k)$ already known of the vascular network, the estimation of absolute statistical blood flow speeds could be made by dividing the measured $\text{Var}(Y)$ by $\text{Var}(k)$ (Fig. 3e). Note that $\text{Var}(Y_s)$ is assumed 0 in simulation.

Finally, our findings showed partial support for Briers et al.'s method of converting measured ICT values to absolute blood flow speeds. Specifically, the conversion is performed by $v_c = \lambda/(2\pi\tau_c)$ where v_c is named decorrelation velocity, λ is wavelength and τ_c is correlation time[16,17]. Our theory shows that this is in fact acquired by assuming $\text{Var}(Y_s) = 0$ and approximating $\text{Var}(k)$ with k_0^2, the square of wavenumber (Eq. 9).

4.2. Interpretation and practical implications of $\text{Var}(k)$

$\text{Var}(k)$ can be interpreted at both the microscopic and macroscopic scales. Microscopically, by definition (Eq. 6 and 8), it provides an essential characterization for the variation of photons' dynamic scattering process inside the probed medium in terms of the accumulated frequency shift. Macroscopically, as revealed by Eq. 9, it reflects the ability of the probed vascular network to induce a decrease of speckle contrast or increase of ICT for a given illumination and detection setup. The micro and macro-scale interpretations are connected due to the fact that photons' dynamic scattering is mainly constrained within the vascular network.

$\text{Var}(k)$ also illustrates that it is challenging, if not impossible, to do absolute blood flow speed measurements through a generalized calibration since $\text{Var}(k)$ is unique for a given vascular network. When the probed vasculature changes, $\text{Var}(k)$ also changes.

4.3. Physical mechanism and practical implications of the directionality susceptibility

The different sensitivity of ICT to the blood flow speed in x-y plane vessels and z-directional descending/ascending vessels is likely due to the different flow direction in those vessels. One might argue that in descending/ascending vessels, the ratio of blood volume in the overall volume sampled by detected photons might be larger than that in the surface vessels. And it might be the larger blood volume ratio in descending/ascending vessels that is causing the higher sensitivity of ICT to the blood flow. We exclude this theory

by manipulating the flow direction in simulation. If the blood volume ratio theory is true, then $\mathrm{Var}\,(k)$ of z-directional vessels should remain larger than that of x-y plane vessels even if the direction of flow is changed since the blood volume ratio is invariant. However, it is observed that $\mathrm{Var}\,(k)$ of the z-directional vascular geometry is smaller than that of y-direction vascular geometry after switching the flow direction in z-directional vascular geometry to y-direction and that in y-directional vascular geometry to z-direction (Table S2). Validation on the realistic vascular geometry shows consistent results (Fig. 6). The bright blobs originally present in the $\mathrm{Var}\,(k)$ map (Fig. 3b) are removed after the amplitudes of y and z component of the unit velocity vector of blood flow are swapped (Fig. 6a). Instead, the position of y-directional vessels is highlighted. However, such phenomena would not appear if it is the amplitudes of x and y component that are swapped (Fig. 6b).
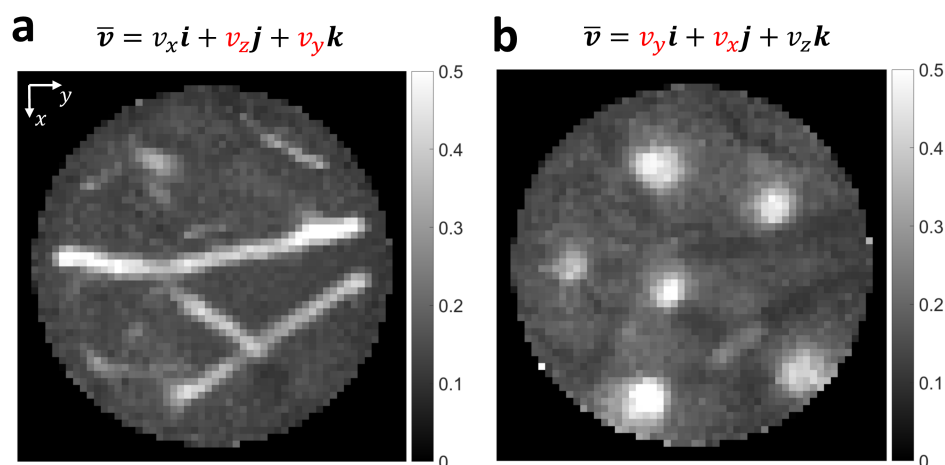

Figure 6: **Map of** $\mathrm{Var}\,(k)$ **with the blood flow direction switched in realistic vascular geometry. a** The amplitudes of y and z components of the unit velocity vector of blood flow are swapped in simulation. **b** The amplitudes of x and y components of the unit velocity vector of blood flow are swapped in simulation.

$\mathrm{Var}\,(k)$ not only quantifies and reveals the directionality susceptibility of LSCI to vessel orientation, but also helps explain such susceptibility. Since $\mathrm{Var}\,(k)$ measures the overall variance of k of detected photons, it is susceptible to the range determined by the extreme values of k. Consider extreme values of k of singly scattered photons first where $k = |\vec{q}|\cos\alpha$. Under normal

illumination, $|\vec{q}| \approx 2k_0$ and $\vec{q}$ is along the z-axis. Therefore, k would be maximized when $\cos\alpha$ is maximized. Since α is the angle between velocity vector $\vec{v}$ and momentum transfer vector $\vec{q}$ which is along the z-axis, $\cos\alpha$ would be maximized when $\vec{v}$ is also along the z-axis. That explains why z-directional vessels have larger $\mathrm{Var}\,(k)$ values than x-y plane surface vessels. Finally, for photons that are scattered multiple times, the randomized directions of $\vec{q}$ and $\vec{v}$ make it difficult to generate extreme k values since the effects of multiple scattering events can cancel out with each other. Hence, the directionality susceptibility mainly originates from the directionality susceptibility retained in single-scattering or few-scattering components of the detected light.

The directionality susceptibility of LSCI has several practical implications. First, direct comparison of ICT values in x-y plane vessels and in ascending/descending vessels should be avoided. If a descending/ascending vessel exhibits a larger ICT value, it does not necessarily imply a higher blood flow than its surface counterpart. Second, the special property of z-directional vessels, i.e., enhanced ability to induce the decrease of speckle contrast and increase of ICT under the same blood flow speed, might be useful in locating descending/ascending vessels. Note that those types of vessels are particularly prevalent in cerebral cortex and play an important role in the blood supply to deeper tissues.

5. Conclusion

The interpretation of ICT is a key topic in quantitative LSCI. Though it has been mainly considered as a metric of blood flow, there is increasing evidence that it is susceptible to the structure of vascular network. We build a theoretical framework to facilitate the modeling of the vascular network's impact on ICT and find that ICT is modulated by vessel orientation. In both simulation and *in vivo* experimental validation, ICT of descending/ascending vessels exhibits a higher sensitivity to blood flow changes than in surface-extending vessels. The different sensitivity is shown due to the flow direction instead of blood volume ratio by simulation. The single-scattering component of the detected light might play a major role in ICT's susceptibility to vessel orientation. Those results suggest that the impact of vascular network structure warrants more attention and investigation in the interpretation of ICT.

Acknowledgements

Author Contributions

Q.F. and A.K.D. developed the theory and designed the experiments; Q.F. and C.Z.J did the Monte Carlo simulation experiments; S.E. and A.T performed the *in vivo* mice imaging experiments; Q.F., C.Z.J, A.T., S.E. and A.K.D wrote the paper together.

Conflicts of Interest

The authors declared no conflicts of interest.

References

[1] AF Fercher and J David Briers. "Flow visualization by means of single-exposure speckle photography". In: *Optics communications* 37.5 (1981), pp. 326–330.

[2] David A Boas and Andrew K Dunn. "Laser speckle contrast imaging in biomedical optics". In: *Journal of biomedical optics* 15.1 (2010), p. 011109.

[3] Andrew K Dunn. "Laser speckle contrast imaging of cerebral blood flow". In: *Annals of biomedical engineering* 40.2 (2012), pp. 367–377.

[4] Joseph W Goodman. "Statistical properties of laser speckle patterns". In: *Laser speckle and related phenomena*. Springer, 1975, pp. 9–75.

[5] Joseph W Goodman. *Speckle phenomena in optics: theory and applications*. Roberts and Company Publishers, 2007.

[6] Wido Heeman et al. "Clinical applications of laser speckle contrast imaging: a review". In: *Journal of biomedical optics* 24.8 (2019), p. 080901.

[7] J David Briers. "Laser speckle contrast imaging for measuring blood flow". In: (2007).

[8] Mitchell A Davis, SM Shams Kazmi, and Andrew K Dunn. "Imaging depth and multiple scattering in laser speckle contrast imaging". In: *Journal of biomedical optics* 19.8 (2014), p. 086001.

[9] Shuai Yuan et al. "Determination of optimal exposure time for imaging of blood flow changes with laser speckle contrast imaging". In: *Applied optics* 44.10 (2005), pp. 1823–1830.

[10] Pavel Zakharov et al. "Quantitative modeling of laser speckle imaging". In: *Optics letters* 31.23 (2006), pp. 3465–3467.

[11] Donald D Duncan and Sean J Kirkpatrick. "Can laser speckle flowmetry be made a quantitative tool?" In: *JOSA A* 25.8 (2008), pp. 2088–2094.

[12] David Briers et al. "Laser speckle contrast imaging: theoretical and practical limitations". In: *Journal of biomedical optics* 18.6 (2013), p. 066018.

[13] Hao Li et al. "Directly measuring absolute flow speed by frequency-domain laser speckle imaging". In: *Optics express* 22.17 (2014), pp. 21079–21087.

[14] Annemarie Nadort et al. "Quantitative blood flow velocity imaging using laser speckle flowmetry". In: *Scientific reports* 6.1 (2016), pp. 1–10.

[15] J Buijs, J van der Gucht, and J Sprakel. "Fourier transforms for fast and quantitative Laser Speckle Imaging". In: *Scientific reports* 9.1 (2019), pp. 1–9.

[16] J David Briers and S Webster. "Quasi real-time digital version of single-exposure speckle photography for full-field monitoring of velocity or flow fields". In: *Optics communications* 116.1-3 (1995), pp. 36–42.

[17] J David Briers and Sian Webster. "Laser speckle contrast analysis (LASCA): a nonscanning, full-field technique for monitoring capillary blood flow". In: *Journal of biomedical optics* 1.2 (1996), pp. 174–180.

[18] Andrew K Dunn et al. "Dynamic imaging of cerebral blood flow using laser speckle". In: *Journal of Cerebral Blood Flow & Metabolism* 21.3 (2001), pp. 195–201.

[19] Ashwin B Parthasarathy et al. "Laser speckle contrast imaging of cerebral blood flow in humans during neurosurgery: a pilot clinical study". In: *Journal of biomedical optics* 15.6 (2010), p. 066030.

[20] Lisa M Richards et al. "Intraoperative laser speckle contrast imaging for monitoring cerebral blood flow: results from a 10-patient pilot study". In: *Photonic Therapeutics and Diagnostics VIII*. Vol. 8207. International Society for Optics and Photonics, p. 82074L.

[21] SM Shams Kazmi et al. "Expanding applications, accuracy, and interpretation of laser speckle contrast imaging of cerebral blood flow". In: *Journal of Cerebral Blood Flow Metabolism* 35.7 (2015), pp. 1076–1084.

[22] Ashwin B Parthasarathy et al. "Robust flow measurement with multi-exposure speckle imaging". In: *Optics express* 16.3 (2008), pp. 1975–1989.

[23] Syed Mohammad Shams Kazmi et al. "Chronic imaging of cortical blood flow using Multi-Exposure Speckle Imaging". In: *Journal of Cerebral Blood Flow Metabolism* 33.6 (2013), pp. 798–808.

[24] SM Shams Kazmi, Satyajit Balial, and Andrew K Dunn. "Optimization of camera exposure durations for multi-exposure speckle imaging of the microcirculation". In: *Biomedical optics express* 5.7 (2014), pp. 2157–2171.

[25] Dmitry D Postnov et al. "Dynamic light scattering imaging". In: *Science advances* 6.45 (2020), eabc4628.

[26] SM Shams Kazmi et al. "Flux or speed? Examining speckle contrast imaging of vascular flows". In: *Biomedical optics express* 6.7 (2015), pp. 2588–2608.

[27] Ingemar Fredriksson and Marcus Larsson. "Vessel packaging effect in laser speckle contrast imaging and laser Doppler imaging". In: *Journal of Biomedical Optics* 22.10 (2017), p. 106005.

[28] Chakameh Z. Jafari et al. "Effect of vascular structure on laser speckle contrast imaging". In: *Biomedical Optics Express* 11.10 (2020), pp. 5826–5841.

21

[29] Bruce J Berne and Robert Pecora. *Dynamic light scattering: with applications to chemistry, biology, and physics.* Courier Corporation, 2000.

[30] Dave J Pine et al. "Diffusing-wave spectroscopy: dynamic light scattering in the multiple scattering limit". In: *Journal de Physique* 51.18 (1990), pp. 2101–2127.

[31] Ranjini Bandyopadhyay et al. "Speckle-visibility spectroscopy: A tool to study time-varying dynamics". In: *Review of scientific instruments* 76.9 (2005), p. 093110.

[32] Pavel Zakharov and Frank Scheffold. "Advances in dynamic light scattering techniques". In: *Light Scattering Reviews 4.* Springer, 2009, pp. 433–467.

[33] Mitchell A Davis et al. "Sensitivity of laser speckle contrast imaging to flow perturbations in the cortex". In: *Biomedical optics express* 7.3 (2016), pp. 759–775.

[34] Mitchell A Davis and Andrew K Dunn. "Dynamic light scattering Monte Carlo: a method for simulating time-varying dynamics for ordered motion in heterogeneous media". In: *Optics express* 23.13 (2015), pp. 17145–17155.

[35] David A Boas and Arjun G Yodh. "Spatially varying dynamical properties of turbid media probed with diffusing temporal light correlation". In: *JOSA A* 14.1 (1997), pp. 192–215.

[36] Tongcang Li et al. "Measurement of the instantaneous velocity of a Brownian particle". In: *Science* 328.5986 (2010), pp. 1673–1675.

[37] Ingemar Fredriksson, Carina Fors, and Johannes Johansson. "Laser doppler flowmetry-a theoretical framework". In: *Department of Biomedical Engineering, Linköping University* (2007), pp. 6–7.

[38] Dilleys Ferreira et al. "Connecting field and intensity correlations: The Siegert relation and how to test it". In: *American Journal of Physics* 88.10 (2020), pp. 831–837.

[39] David A Boas et al. "Establishing the diffuse correlation spectroscopy signal relationship with blood flow". In: *Neurophotonics* 3.3 (2016), p. 031412.

[40] Samuel A Mihelic et al. "Segmentation-Less, Automated, Vascular Vectorization". In: *PLOS Computational Biology* 17.10 (2021), e1009451.

[41] Blender Online Community. *Blender - a 3D modelling and rendering package*. Blender Foundation. Stichting Blender Foundation, Amsterdam, 2018.

[42] Annie Zhou et al. "Evaluation of resonant scanning as a high-speed imaging technique for two-photon imaging of cortical vasculature". In: *Biomedical Optics Express* 13.3 (2022), pp. 1374–1385.

[43] Shaun A Engelmann et al. "Diamond Raman laser and yb fiber amplifier for in vivo multiphoton fluorescence microscopy". In: *Biomedical Optics Express* 13.4 (2022), pp. 1888–1898.

[44] Vinayakrishnan Rajan et al. "Review of methodological developments in laser Doppler flowmetry". In: *Lasers in medical science* 24.2 (2009), pp. 269–283.